Fizika Nizkikh Temperatur, 2007, v. 33, No. 1, p. 78–87

Magnetic and transport properties driven by lattice strain in $La_{0.7}Ca_{0.3}MnO_3/BaTiO_3$ and $La_{0.7}Sr_{0.3}MnO_3/BaTiO_3$ bilayered films

V.G. Prokhorov, V.A. Komashko, and G.G. Kaminsky

Institute of Metal Physics of the National Academy of Sciences of Ukraine, Kiev 03142, Ukraine
E-mail: pvg@imp.kiev.ua

K.K. Yu, S.J. Jun, S.Y. Park, J.S. Park, and Y.P. Lee

q-PSI and Department of Physics, Hanyang University, Seoul 133-791, Korea

V.L. Svetchnikov

National Center for HREM, TU Delft, 2628AL, The Netherlands

Received February 3, 2006, revised March 13, 2006

The microstructure and the magnetic and transport properties of $La_{0.7}Ca_{0.3}MnO_3$ and $La_{0.7}Sr_{0.3}MnO_3$ films deposited on a $BaTiO_3$ layer (LCMO/BTO and LSMO/BTO) and on a $LaAlO_3$ (001) single crystal (LCMO/LAO and LSMO/LAO) by rf-magnetron sputtering using «soft» (or powder) targets are investigated. The films grown on BTO demonstrate biaxial tensile in-plane and compressive out-of-plane strains, while the films grown on LAO, in contrast, manifest compressive in-plane and tensile out-of-plane strains. The films with biaxial tensile in-plane lattice strain undergo the magnetic transition at a higher temperature than that for the biaxial compressive case. This argues that the Mn–O–Mn bond-angle variation, controlled by the lattice strain, plays a more important role in the formation of the spin ordering than the attendant modification of the Mn–O bond length. It was shown that the magnetic inhomogeneity, expressed by a significant difference between the field-cooled and zero-field-cooled temperature-dependent magnetization, has a metallurgical rather than an electronic nature, and is controlled by the crystal lattice distortion and the microstructure defects. The observed enhancement of the magnetoresistance effect in the LSMO/BTO bilayer at room temperature make this object greatly beneficial in the development of new hybrid ferromagnetic/ferroelectric devices.

PACS: **71.30.+h**, 75.47.Gk, 75.47.Lx

Keywords: magnetotransport properties, ferromagnetic/ferroelectric films, microstructure peculiarities.

1. Introduction

The discovery of colossal magnetoresistance (CMR) in doped manganite perovskites [1] with the general formula $R_{1-x}A_xMnO_3$, where R is a rare-earth cation and A is an alkali or alkaline earth cation [2,3], has stimulated numerous investigations not only because of their interesting fundamental science but because of possibilities for device applications. For a great number of these potential industrial applications, these materials have to be prepared in the form of thin films or multilayered hybrid systems. However, the manganite thin films frequently show different magnetotransport properties in comparison to bulk materials. The observed discrepancy is mainly explained by the accumulation of lattice strain due to the epitaxial growth of the film, which plays an important role in formation of the spin-ordered state and the value of CMR effect [4–13]. It has been declared, for example, that a lattice compression will reduce the electron–phonon interaction and increase the electronic hopping amplitude by decreasing the Mn–O bond

length while increasing the Mn–O–Mn bond angle, all leading to increase of the Curie temperature T_C. In contrast, the Jahn–Teller distortion will lead to a localization of electrons and reduce T_C [4]. This phenomenon is described, as a rule, on the basis of the Millis model [14], developed for materials with weak lattice strains and a cubic symmetry. On the other hand, the recently observed suppression of the contribution from the Jahn–Teller distortion to the ferromagnetic ordering with increasing lattice mismatch between substrate and film [7,12,13,15,16] demonstrates a physical limitation of the weak-strain approach [14] in describing the magnetic properties of manganite films. Moreover, it has been shown that the microstructure features [9,16–18] and the oxygen content [6,19–25] can lead to considerable change in the magnetotransport properties of the films, as well.

In spite of the fact that the influence of kind of single-crystalline substrates on the magnetic and the electronic properties of manganite films has been quite well investigated, the development of hybrid devices such as ferromagnetic/ferroelectric ones, which are very promising for modern applications [26], needs detailed information on the microstructure of interfaces and the mutual influence between heterogeneous layers.

In this paper, we report the experimental results for the LCMO/BTO and the LSMO/BTO hybrid ferromagnetic/ferroelectric films. For comparison, we present the same data for the films deposited on the bare LAO and $SrTiO_3$ (STO) substrates. The observed difference in the growth mechanism of the LCMO and the LSMO films and the influence of the lattice strain and the microstructure peculiarities on the magnetotransport properties are discussed in detail.

2. Experimental techniques

The films were prepared by an on-axis rf-magnetron sputtering using a so-called «soft» (or powder) target [27]. The substrate was a LAO (001) single crystal with an out-of-plane lattice parameter of $c \simeq 0.379$ nm for the pseudocubic symmetry. The total pressure in chamber was $4 \cdot 10^{-2}$ Torr with a gas mixture of Ar and O_2 (2:1). The substrate temperature during deposition was 750 °C. The LCMO/BTO and the LSMO/BTO bilayers were prepared with thicknesses for LCMO, LSMO, and BTO of $d \simeq 160$, 160, and 100 nm, respectively. For comparison, the bare BTO, LCMO, and LSMO films with the same thicknesses were deposited on the LAO substrate at the similar conditions. The LSMO films were prepared with $d \simeq 70$ nm onto the STO substrate as well. The θ–2θ x-ray diffraction (XRD) patterns were obtained using a Rigaku diffractometer with Cu K_α radiation. The high-resolution electron-microscopy (HREM) studies were carried out using a Philips CM300UT-FEG microscope with a field emission gun operated at 300 kV. The point resolution of the microscope was of the order of 0.12 nm. The cross-sectional specimens were prepared by the standard techniques using mechanical polishing followed by ion-beam milling at a grazing incidence. All microstructure studies were carried out at room temperature. The resistance measurements were performed by using four-probe method in a temperature range of 4.2–300 K and a magnetic field up to 5 T. The in-plane field-cooled (FC) and zero-field-cooled (ZFC) magnetization curves under an applied magnetic field of 100 Oe and the magnetization hysteresis loops at 10 K were taken with a Quantum Design SQUID magnetometer.

3. Microstructures of the films

Figure 1,*a* shows the θ–2θ XRD scan for the BTO film deposited on the LAO substrate. The high intensity of the (00*l*) peaks indicates that the deposition results in highly *c*-oriented film. The obtained out-of-plane lattice parameter ($c \simeq 0.407$ nm) is not very different from the bulk value at room temperature, $c \simeq 0.4033$ nm [28]. Figures 1,*b* and 1,*c* display, in detail, the (004) Bragg peaks for the LCMO/BTO and the LCMO/LAO, and the LSMO/BTO and the LSMO/LAO films, respectively. The analysis of XRD data reveals that the out-of-plane lattice param-

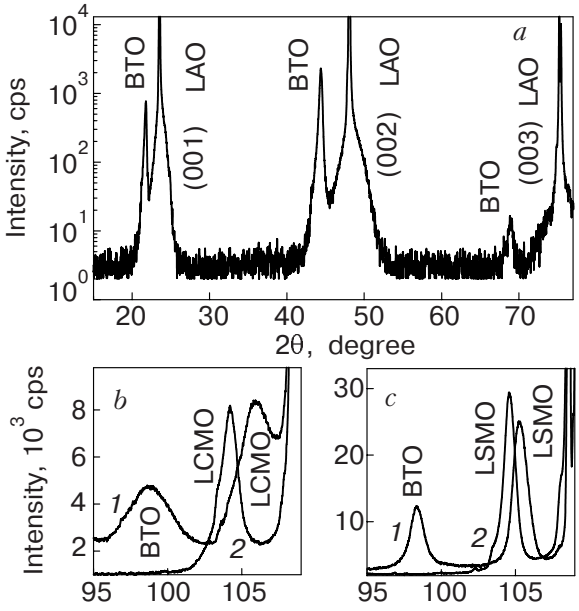

Fig. 1. θ–2θ XRD pattern for the BTO/LAO film (*a*). The (004) Bragg peaks for the LCMO and the LSMO films, respectively, deposited on BTO (*1*) and LAO (*2*) (*b*) and (*c*).

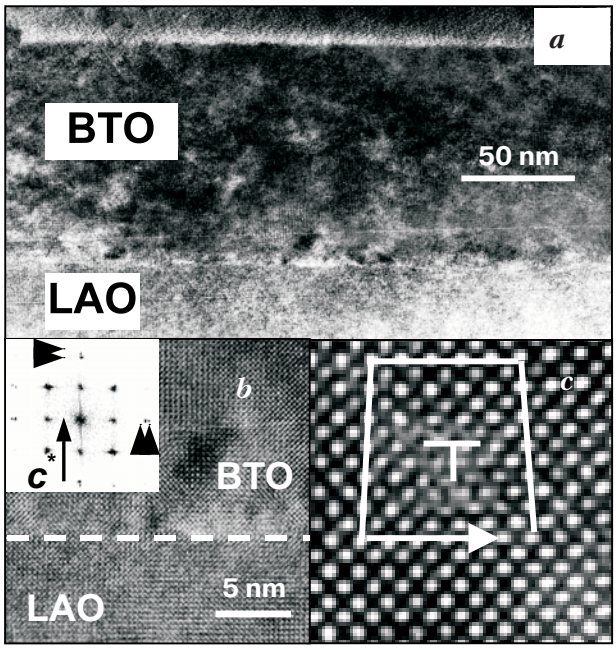

Fig. 2. Low-magnification cross-sectional HREM image for BTO/LAO film (*a*). High-magnification cross-sectional HREM image for the BTO/LAO interface. Dashed line indicates the interface. Inset is corresponding FFT (*b*). The misfit dislocation formed in BTO film near interface. An associated Burgers circuit is indicated by the white line (*c*).

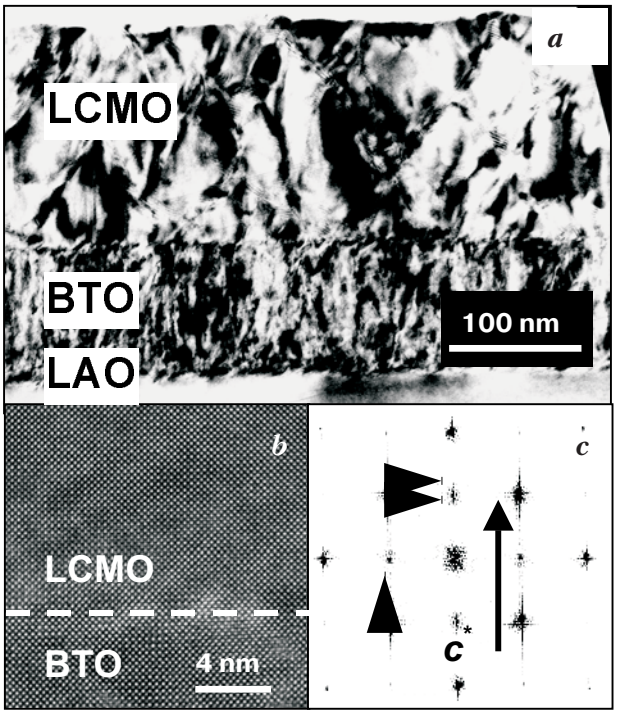

Fig. 3. Low-magnification cross-sectional HREM image for LCMO/BTO film (*a*). High-magnification cross-sectional HREM image of the LCMO/BTO interface. Dashed line indicates the interface (*b*). FFT of the HREM image in Fig. 3,*b* (*c*).

eter for LCMO/LAO corresponds to $c \simeq 0.39$ nm, while $c \simeq 0.3857$ nm for LCMO/BTO. Similar to that $c \simeq 0.3891$ nm for LSMO/LAO while $c \simeq 0.3872$ nm for LSMO/BTO.

Figure 2 presents the low-magnification cross-sectional HREM image of the BTO film (*a*) and the high-magnification one for a region including the BTO/LAO interface (*b*). The inset in Fig. 2,*b* displays the fast Fourier transform (FFT) of the high-magnification HREM image. The FFT of the HREM image across the BTO/LAO interface reveals elongated and slightly split spots in both the *c* (normal to the interface) and *a* (along the interface) directions (indicated by the black arrows in Fig. 2,*b*). This is evidence for the semicoherent (or weakly coherent) lattice coupling between LAO and BTO. Due to the large mismatch between substrate and film, misfit dislocations are formed in BTO near the interface, as is displayed in Fig. 2,*c*. The corresponding Buerger's circuit is indicated by the white line. The measurement of various interspot spacings on the high-magnification HREM image allows us to obtain average values of the lattice parameters. Analysis reveals that the BTO film has a tetragonal crystal lattice with $c \simeq$ $\simeq 0.407$ nm and $c/a \simeq 1.02$. The obtained lattice parameters are almost coincident with those for the bulk [28] and for the BTO films deposited on $SrTiO_3$ ($a \simeq 0.3905$ nm) [29].

Figure 3 presents (*a*) the low- and (*b*) high-magnification cross-sectional HREM images of the LCMO/BTO bilayered film. It is seen that FFT (*c*) of the LCMO/BTO HREM image across the interface produces a rectangular pattern of the spots, which are elongated only along the out-of-plane direction without a visible splitting or an elongation in the in-plane direction. This indicates that almost coherent interface is formed between BTO and LCMO. Analysis of the interspot spacings and the angles between spot rows and columns reveals that the LCMO layer has a tetragonal crystal structure with $c \simeq 0.386$ nm, which is in good agreement with the XRD data, and has a reversed (with respect to BTO) tetragonal ratio, $c/a \simeq 0.98$. The estimated in-plane lattice parameter for LCMO, $a \simeq 0.394$ nm, turns out to be very close to that for BTO, $a \simeq 0.399$ nm.

For comparison a similar microstructural analysis has been carried out for the LCMO film deposited directly on LAO, which is represented by Fig. 4. FFT in this case produces a rectangular pattern similar to that for the LCMO/BTO interface, with a well-defined spot splitting in the out-of-plane direction and slightly elongated spots along the in-plane direction, mani-

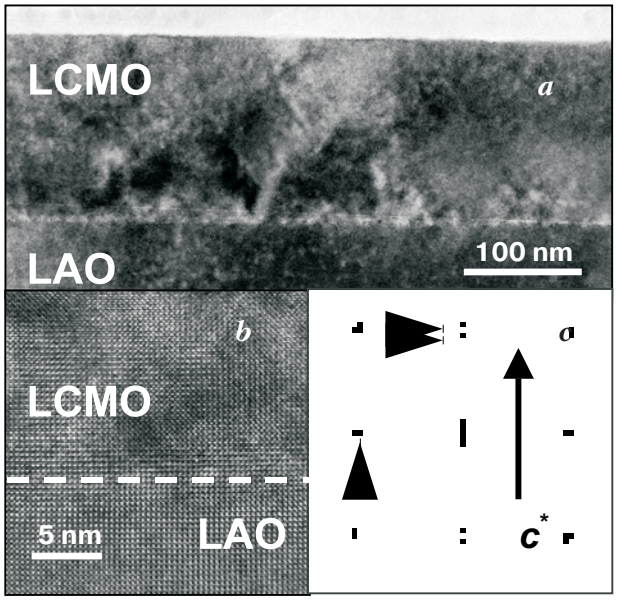

Fig. 4. Low-magnification cross-sectional HREM image for LCMO/LAO film (*a*). High-magnification cross-sectional HREM image of the LCMO/LAO interface. Dashed line indicates the interface (*b*). FFT of the HREM image in Fig. 4,*b* (*c*).

festing a nearly coherent interface between the film and the substrate. The LCMO/LAO film reveals a tetragonal crystal lattice with $c \simeq 0.39$ nm, which is perfectly coincident with the corresponding XRD data, and $c/a \simeq 1.015$.

The same cross-sectional HREM images for LSMO/BTO and LSMO/LAO are represented in Figs. 5 and 6, respectively. For both films the FFTs result in the slightly elongated spots along both the in-plane and the out-of-plane directions. The analysis of the high-magnification HREM images reveals that the tetragonal distortion of the LSMO layers is significantly smaller then that for LCMO ones: $c/a \simeq 0.996$ for LSMO/BTO and $c/a \simeq 1.008$ for LSMO/LAO. Insets in Figs. 5,*b* and 6,*b* display moire patterns (inverse Fourier transforms [30]) of the high-magnification HREM images across interface for LSMO/BTO and LSMO/LAO, respectively. It is seen that in both cases the edge dislocations are formed in the LSMO film (noted by white arrows). Moreover, these dislocations can be of opposite sign. Therefore, one can conclude that a semicoherent interface between the substrate and film is formed in the deposition of LSMO.

The lattice parameters and the estimated values of the in-plane ($\varepsilon_{100} = (a_{\text{bulk}} - a_{\text{film}})/a_{\text{bulk}}$) and out-of-plane ($\varepsilon_{001} = (c_{\text{bulk}} - c_{\text{film}})/c_{\text{bulk}}$) lattice strains for investigated samples are summarized in Table 1. Table 1 also contains the data for the LSMO/STO

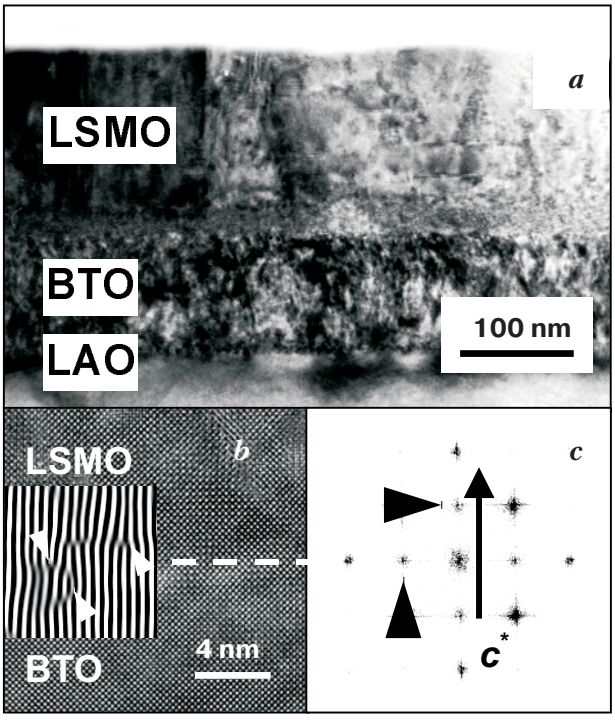

Fig. 5. Low-magnification cross-sectional HREM image for LSMO/BTO film (*a*). High-magnification cross-sectional HREM image of the LSMO/BTO interface. Dashed line indicates the interface. Inset shows moire pattern across the interface with misfit dislocations (indicated by white arrows) (*b*). FFT of the HREM image in Fig. 5,*b* (*c*).

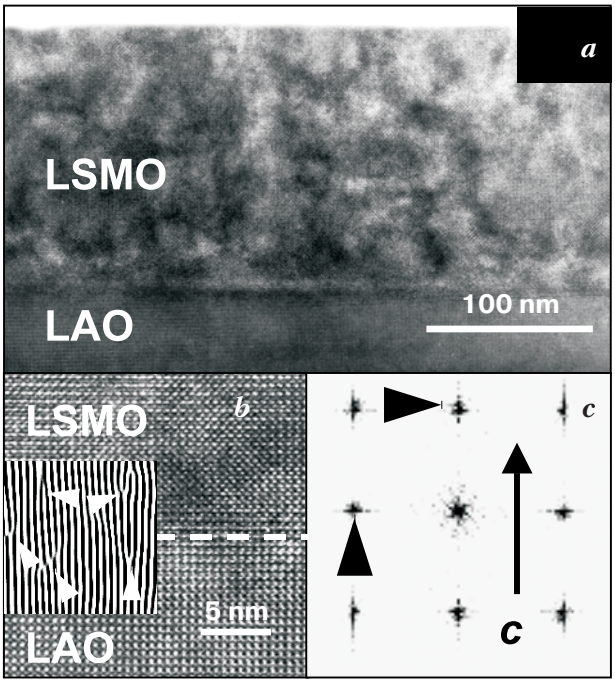

Fig. 6. Low-magnification cross-sectional HREM image for LSMO/LAO film (*a*). High-magnification cross-sectional HREM image of the LSMO/LAO interface. Dashed line indicates the interface. Inset shows moire pattern across the interface with misfit dislocations (indicated by white arrows) (*b*). FFT of the HREM image in Fig. 6,*b* (*c*).

Table 1. Results of the XRD and the HREM analysis for the investigated films.

Samples	Out-of-plane lattice parameter, c (nm), XRD data	Tetragonal ratio, c/a, HREM data	In-plane strain, ε_{100} (%)	Out-of-plane strain, ε_{001} (%)	Bulk strain, ε_B (%)*	Jahn–Teller strain, ε_{JT} (%)**
BTO/LAO	0.407	1.02	0.12	−0.92	−0.68	−0.84
LCMO/BTO	0.3857	0.99	−0.93	0.46	−1.4	1.14
LCMO/LAO	0.39	1.015	0.57	−0.64	0.49	−1.0
LSMO/BTO	0.3872	0.996	−0.36	0.53	−0.2	0.73
LSMO/LAO	0.3891	1.008	0.6	−0.19	1.01	−0.65
LSMO/STO	0.3869	0.993	−0.1	0.6	0.41	0.57
LSMO/BTO***	0.3864	0.98	−1.29	0.73	−1.86	1.66
LSMO/LAO***	0.3903	1.01	0.72	−0.27	1.17	−0.81

Notes: * — $\varepsilon_B = (2\varepsilon_{100} + \varepsilon_{001})$; ** — $\varepsilon_{JT} = \sqrt{2/3}(\varepsilon_{001} - \varepsilon_{100})$; *** — thickness of the LSMO layer is $d \simeq 70$ nm.

film with $d \simeq 160$ nm and for the LSMO/BTO and the LSMO/LAO thin ($d \simeq 70$ nm) films, for comparison. The following lattice parameters for bulk were employed in this evaluation: $a_{\text{bulk}} \simeq 0.3864$ nm and $c_{\text{bulk}} \simeq 0.3875$ nm for $La_{0.7}Ca_{0.3}MnO_3$ [31] and $a_R^{\text{bulk}} \simeq 0.548$ nm and $\alpha_R^{\text{bulk}} \simeq 60.3°$ for $La_{0.7}Sr_{0.3}MnO_3$ [32].

Therefore, two kinds of the films with different sign of the lattice strain have been prepared: LCMO/BTO and LSMO/BTO have biaxial tensile in-plane and compressive out-of-plane strains, while LCMO/LAO and LSMO/LAO are subjected reversely, to compressive in-plane and tensile out-of-plane strains. On the other hand, it is seen that the LCMO films are more susceptible to the crystal structure of the substrate and accumulate more lattice strains during deposition in comparison to the LSMO ones. The observed difference in the lattice-strained state for these films can be governed by the peculiarities of the growth mechanism. Recently it was shown that the LSMO films tend toward stress relaxation during growth by the formation of misfit dislocations, while the LCMO films form a column-like strained microstructure [33–35]. This agrees well with our results, which testify that the LCMO films demonstrate a dislocation-free epitaxial growth mode with the formation of a strong lattice-strained state. These biaxial strains accommodate, during the film growth, in forming a coherent columnar microstructure directed along the interface normal which can be treated as prismatic antiphase boundaries. However, in the LSMO films a strain accommodation is realized owing to the formation of misfit dislocations.

4. Magnetic and transport properties

Figure 7 shows the in-plane FC (solid symbols) and ZFC (open symbols) temperature-dependent magnetization curves, $M(T)$, for the LCMO/BTO (*1*) and the LCMO/LAO (*2*) systems. The applied magnetic field was $H = 100$ Oe. The LCMO/BTO bilayer manifests the onset of ferromagnetic ordering at $T_C \simeq 250$ K, while LCMO/LAO has a Curie point at a lower temperature $T_C \simeq 230$ K, which is typical for

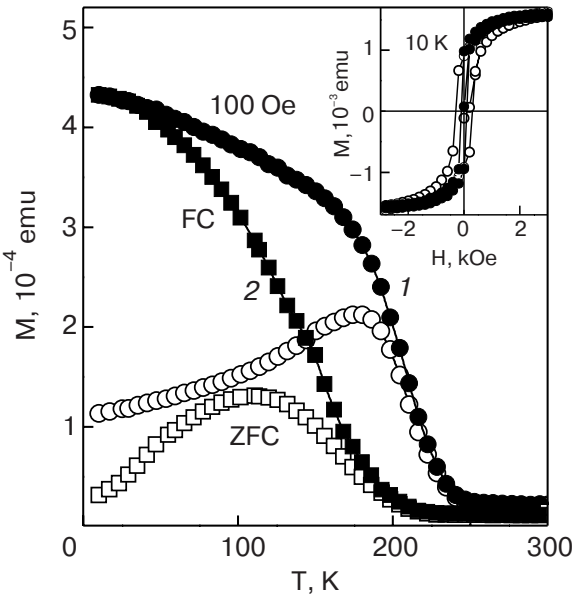

Fig. 7. Temperature dependence of the FC (solid symbols) and ZFC (open symbols) magnetizations for LCMO/BTO (*1*) and LCMO/LAO (*2*). Inset displays the in-plane magnetic hysteresis loops for LCMO/BTO (solid symbols) and LCMO/LAO (open symbols) at 10 K. Lines are a guide to the eye.

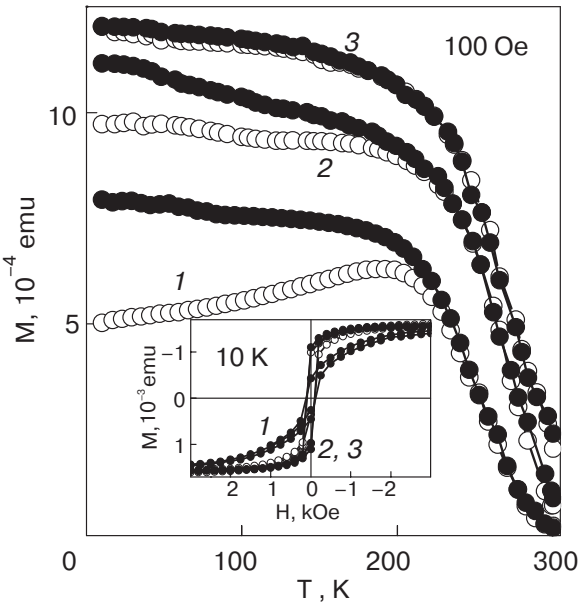

Fig. 8. Temperature dependence of the FC (solid symbols) and ZFC (open symbols) magnetizations for LSMO/LAO (*1*), LSMO/BTO (*2*), and LSMO/STO (*3*). Inset displays the in-plane magnetic hysteresis loops at 10 K. Lines are a guide to the eye.

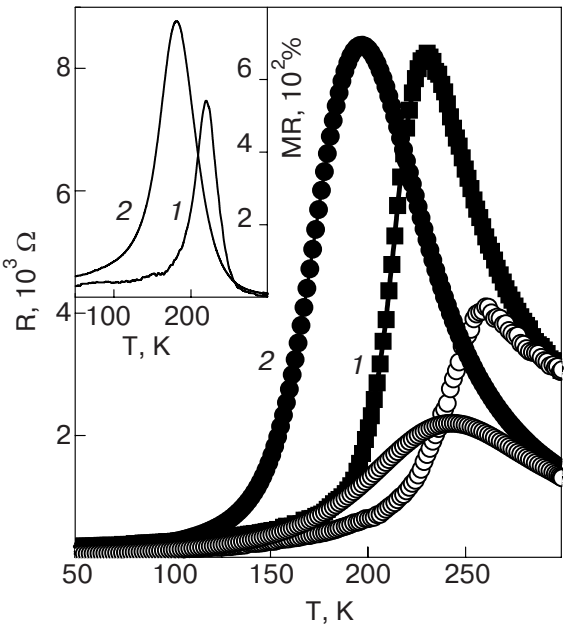

Fig. 9. Temperature dependence of the resistance for LCMO/BTO (*1*) and LCMO/LAO (*2*) without (solid symbols) and with (open symbols) an applied magnetic field of 5 T. Inset includes the temperature-dependent MR ratios. Lines are a guide to the eye.

the lattice-strained as-deposited film [9,10,12,36]. The inset in Fig. 7 displays the in-plane magnetic hysteresis loops, measured at T = 10 K, for the LCMO/BTO (solid symbols) and the LCMO/LAO (open symbols) films. The $M(H)$ for LCMO/BTO is narrower (the coercive field is $H_c \simeq 100$ Oe) and saturates twice as fast (the saturation field is $H_s \simeq \simeq 3000$ Oe), as compared to LCMO/LAO ($H_c \simeq \simeq 300$ Oe and $H_s \simeq 6000$ Oe) which can be explained by a strain-driven magnetic anisotropy in these films [5,37].

Figure 8 displays the similar magnetization dependencies for LSMO/LAO (*1*), LSMO/BTO (*2*), and LSMO/STO (*3*) films. The maximal temperature of the ferromagnetic ordering is observed for LSMO/STO, $T_C \simeq 315$ K, while the lowest one belongs to LSMO/LAO, $T_C \simeq 296$ K. The LSMO/BTO film has $T_C \simeq 310$ K. The inset in Fig. 8 shows that the coercive field is the same for all the LSMO films, $H_c \simeq 100$ Oe, while the saturation field is considerably dependent on the substrate: $H_s \simeq 4000$, 1200, and 800 Oe for LSMO/LAO, LSMO/STO, and LSMO/BTO, respectively.

Figure 9 is the temperature-dependent resistance, $R(T)$, for the LCMO/BTO (1) and the LCMO/LAO (*2*) films without (solid symbols) and with (open symbols) an applied magnetic field of 5 T. The magnetic field was directed parallel to the film surface and at right angles to the transport current. It is seen that the LCMO/BTO bilayer undergoes the metal–insulator (MI) transition at $T_P \simeq 230$ K, while the LCMO/LAO film manifests $T_P \simeq 195$ K. In both cases the temperature of MI transition is lower than the corresponding Curie point and understood by a percolating nature of the MI transition [38]. The inset in Fig. 9 presents the temperature dependence of negative magnetoresistance (MR) for LCMO/BTO (*1*) and LCMO/LAO (*2*). The MR value is defined by 100% × $[R(0) - R(H)]/R(H)$, where $R(0)$ and $R(H)$ are the resistances without and with a magnetic field of 5 T.

Figure 10 displays the similar $R(T)$ dependencies without (solid symbols) and with (open symbols) an applied magnetic field of 5 T for the thin ($d \simeq 70$ nm) LSMO/LAO (*1*) and LSMO/BTO (*2*), and thick ($d \simeq 160$ nm) LSMO/BTO (*3*) and LSMO/LAO (*4*) films. Inset (*a*) shows the temperature dependence of the MR value for these films. Because the LSMO manganite does not undergo a real MI transition near the Curie point and manifests only a change in the slope of the $R(T)$ dependence, the MI temperature was obtained from analysis of the first derivative of $R(T)$ versus T curves, which are presented in the inset (*b*). It is seen that for thick LSMO/BTO and LSMO/LAO $T_P \simeq 275$ and 250 K, while for thin ones $T_P \simeq 260$ and 220 K, respectively (denoted by ar-

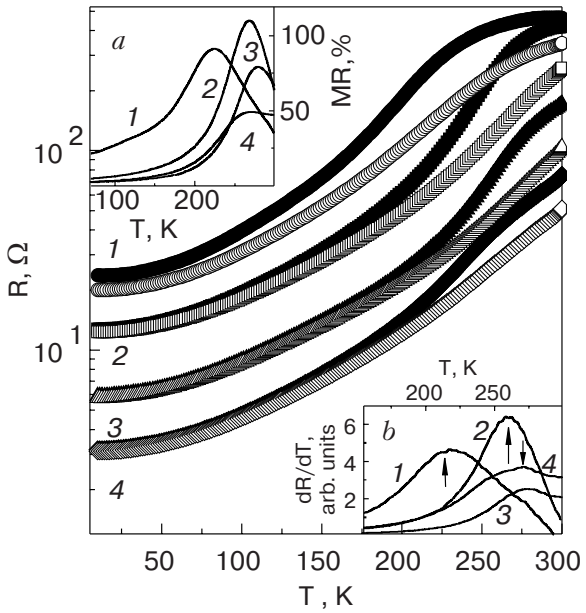

Fig. 10. Temperature dependence of the resistance for LSMO/LAO (*1*) and LSMO/BTO (*2*) with d = 70 nm, and LSMO/BTO (*3*) and LSMO/LAO (*4*) with d = = 160 nm without (solid symbols) and with (open symbols) an applied magnetic field of 5 T. Inset (*a*) includes the temperature-dependent MR ratios. Inset (*b*) displays the temperature-dependent first derivative dR/dT. (MI transition temperatures indicated by arrows).

rows). Some of the magnetotransport characteristics for the investigated films are summarized in Table 2.

5. Discussion

Let us analyse the obtained results on the basis of Millis model [14]. For weak lattice strain and a cubic symmetry T_C can be expressed by:

$$T_C(\varepsilon) = T_C(\varepsilon = 0)\left(1 - \alpha\varepsilon_B - \frac{1}{2}\Delta\varepsilon_{JT}^2\right),$$

where $\alpha = (1/T_C)(dT_C/d\varepsilon_B)$, and $\Delta = (1/T_C) \times$ $\times (d^2T_C/d\varepsilon_{JT}^2)$, ($dT_C/d\varepsilon_{JT} = 0$ by cubic symmetry). The magnitudes of α and Δ represent the relative weights for the symmetry-conserving bulk and the symmetry-breaking Jahn–Teller strains, respectively. Here $\varepsilon_B = (2\varepsilon_{100} + \varepsilon_{001})$ is a bulk strain and $\varepsilon_{JT} = \sqrt{2/3}(\varepsilon_{001} - \varepsilon_{100})$ is a Jahn–Teller strain. Based on the dynamical «mean field» approximation [39] and considering the electron–phonon coupling due to the Jahn–Teller splitting [40], one can calculate numerically the compressive (α) and uniaxial (Δ) strain dependence as function of the elecron–phonon interaction. According to the model [14], $\alpha \simeq 10$ for a reasonable the electron–phonon coupling ($0.5 \le \lambda \le$ ≤ 1) in these compounds, where λ is the electron–phonon interaction constant, and $\Delta \simeq 5000$. Taking into account that the Curie temperature for the strain-free bulk $La_{0.7}Ca_{0.3}MnO_3$ compound is $T_C(\varepsilon = 0) \simeq 265$ K [41], and using the values obtained for ε_B, ε_{JT}, and T_C, we estimated Δ as 3000 and 1500 for LCMO/BTO and LCMO/LAO, respectively, which agree in principle with the model prediction. On the other hand, the same analysis carried out for the LSMO films showed a larger disagreement with theoretical model. The estimated values of Δ change to 7000, 5000, and 800 for LSMO/BTO, LSMO/LAO, and LSMO/STO, respectively. The Curie point of 375 K was used for the strain-free bulk $La_{0.7}Sr_{0.3}MnO_3$ compound [32]. A similar strong discrepancy between the model and the experiment was recently observed for the LCMO films deposited on STO and $NdGaO_3$ [15,16]. The main explanation for this disagreement is based on the existence of a dead layer or parasitic phase located at the film/substrate interface, which leads to an additional influence on the Curie temperature together with lattice strain [15,16,42]. However, the cross-sectional HREM images did not manifest the appearance of any extensive defects close to the interface in the investigated films, and the temperature-dependent magnetization curves attest to the existence a single-phase magnetic state only. We believe that the following main reasons lead to the observed disagreement. The first of them is

Table 2. Magnetotransport characteristics for the investigated films

Samples	Curie point, T_C, K	Coercive field, H_c, Oe	Saturation field, H_S, Oe	Remanence, M_r/M_S, %	Magnetoresistance*, MR, %	MI transition, T_P, K
LCMO/BTO	250	100	3000	61	550 (17)	230
LCMO/LAO	230	300	6000	59	760 (9)	195
LSMO/BTO	310	100	800	73	80 (65)	275
LSMO/LAO	296	100	4000	31	50 (43)	250
LSMO/STO	315	100	1200	70	40 (38)	280

Notes: * — in brackets are MR values at 300 K.

connected with the relatively random selection of the bulk lattice parameters for an estimation of the in-plane and the out-of-plane strains, owing to the strong variations between the experimental data which can be found in the literature [22,31–35,41, 43–45]. Secondly, even annealed strain-free films have different unit cell volume compared to the bulk materials [42,44]. Therefore, we are sure that the correct testing of the Millis model [14] for the CMR films must be carried out using the lattice parameters of the annealed films as the «bulk» rather than those of the real bulk materials.

On the other hand, the elastic stress intensity in these films can be identified with the tetragonal distortion of the crystal lattice. Table 1 shows that the tetragonal ratios are larger for the LCMO than for the LSMO films. This can be explained by the different mechanism of growth of these films. The HREM data reveal that LCMO demonstrates the epitaxial mode, with the formation of an almost coherent interface between the substrate and the film, while the growth of LSMO is accompanied by dislocation formation that results in a semicoherent interface.

Let us consider in detail influence of the lattice strained state and the microstructure features on magnetotransport properties of the investigated films.

Figure 7 shows that LCMO/BTO with a biaxial tensile in-plane lattice strain undergoes the magnetic transition at higher temperature than that observed in LCMO/LAO, with biaxial compressive strains. It is well known that the electronic transfer integral in CMR could be determined mainly by Mn–O bond length and Mn–O–Mn angle [46]. The final result for T_C can be approximately written as $T_C \sim \sim \cos\varphi / d_{\mathrm{Mn-O}}^{3.5}$, where φ is the tilt angle in the plane of the bond, and $d_{\mathrm{Mn-O}}$ is the Mn–O bond length [47,48]. It is believable that the tetragonal elastic deformation of a crystal lattice, provided by compressive and tensile strains, results in a simultaneous change of the Mn–O bond length and the Mn–O–Mn angle, owing to the distorted vertex-sharing of MnO_6 octahedra [49]. Taking into account that the biaxial tensile in-plane lattice strain increases the Mn–O bond length, it would be reasonable to expect a significant lowering of the Curie point for the LCMO/BTO film, in disagreement with the experimental results. Therefore, one can conclude that the variation of the Mn–O–Mn bond angle, controlled by a lattice strain, plays more important role in the formation of the spin ordering in the CMR film than the attendant modification of the Mn–O bond length.

Table 2 shows that the LCMO/BTO film has a lower saturation field and larger remanent magnetization as compared with the LCMO/LAO film. This effect is provided by the magnetic anisotropy of strained epitaxial films, which is strongly correlated with the nature of the substrate-induced lattice strain states. It was shown that the easy axis magnetization always takes up a position along the direction of the tensile strain [5,8]. Consequently, in the LCMO/BTO film an in-plane biaxial magnetic anisotropy is observed, while the easy axis magnetization is perpendicular to the LCMO/LAO film plane. The observed increase of the coercive field for LCMO/LAO can be connected with the column-like texture of the film [33–35], which can play the role of additional pinning centers for magnetic domain walls during a magnetization reversal.

The LSMO films also demonstrate the influence of the substrate-induced lattice strain on the magnetic properties, but this effect is manifested more slightly in comparison with the LCMO ones. Similar to LCMO, the LSMO/BTO and LSMO/STO films with a biaxial tensile in-plane lattice strain demonstrate higher Curie temperatures than that observed in the LSMO/LAO film. This implies that in the LSMO films the ferromagnetic ordering is governed by the tilt bond angle rather than the Mn–O bond length, as well.

The relatively small value of the saturation field and the high remanence testify that the LSMO films deposited on BTO and STO have in-plane easy-axis magnetization, in contrast to LSMO/LAO, which is also coincident with data for the LCMO films. On the other hand, the coercive field remains the same for all films and does not depend on the substrate material. Therefore, the prepared LSMO films do not have large-size microstructure faults (for example, such as column-like texture in LCMO/LAO [33–35]) that could pin the magnetic domains during magnetization reversal.

Figures 7 and 8 show that the difference between ZFC and FC magnetization curves at low temperature essentially depend on the substrate material. This phenomenon is usually treated as an existence of the intrinsic inhomogeneous magnetic (or «cluster» glass) state governed by the tendency of CMR toward electronic phase separation [38]. Let us to express the degree of magnetic inhomogeneity in the films by $\Delta M_{ZFC}^{FC} = 100\% \times [M^{FC}(T) - M^{ZFC}(T)]/M^{FC}(T)$, where $M^{FC}(T)$ and $M^{ZFC}(T)$ are the FC and ZFC magnetizations at a certain temperature. The ΔM_{ZFC}^{FC} values turn out to be significantly different for the investigated films: 93, 74, 37, 20, and 0% for LCMO/LAO, LCMO/BTO, LSMO/LAO, LSMO/BTO, and LCMO/STO, respectively, at $T \to 0$. The higher degree of magnetic inhomogeneity is observed in the LCMO films with larger tetragonal distortion of crys-

tal lattice (see Table 1) and a columnar microstructure [33–35,50], which is formed through the biaxial in-plane strain accommodation. In contrast to that the LSMO films demonstrate smaller tetragonal distortion of crystal lattice due to introduction of the misfit dislocations during its growth that is resulted in a more regular microstructure and a small degree of magnetic inhomogeneity. Therefore, this kind of magnetic inhomogeneity, which is connected with the observed difference in FC and ZFC $M(T)$ dependences, has a metallurgical rather than an electronic nature, and is controlled by the crystal lattice distortion and the microstructure defects.

The temperature dependencies of resistance represented by Figs. 9 and 10 manifest mainly a typical for the CMR films behavior. For example, the MI transition temperature, which is treated as a peak on the $R(T)$ curve (for the LSMO films it is a peak on the first derivative $dR(T)/dT$ curve), is strongly correlated with the Curie point and in our case can be expressed by a simple empirical relation: $T_P \simeq 0.92T_C - 11.6$ K. On the other hand, the usual increase of the MR value with decreasing T_P is observed only for the LCMO films. Insets (*a*) and (*b*) in Fig. 10 show that the LSMO/BTO films demonstrate larger MR values in comparison to the LSMO/LAO ones, though their MI transition temperatures are higher, as well. Thus, MR = 80 and 110%, and $T_P \simeq 275$ and 260 K for LSMO/BTO with $d \simeq 160$ and 70 nm, respectively, while MR = 50 and 91%, and $T_P \simeq 250$ and 220 K for LSMO/LAO with $d \simeq 160$ and 70 nm, respectively. Therefore, the deposition of the LSMO film on the BTO layer leads to an increase of the magnetoresistance effect. Moreover, the LSMO/BTO bilayered film demonstrates the maximal MR value at room temperature: $\simeq 65\%$.

6. Conclusions

We have performed magnetotransport measurements on LCMO/BTO and LSMO/BTO bilayered films deposited by rf-magnetron sputtering, using «soft» (or powder) targets. For comparison, LCMO/LAO, LSMO/LAO, and LSMO/STO films have been prepared as well. The HREM analysis reveals: (i) first, the BTO layer has a tetragonal crystal lattice, *c*-oriented along the normal to the film plane; (ii) second, LCMO/BTO and LSMO/BTO have biaxial tensile in-plane and compressive out-of-plane strains, while LCMO/LAO and LSMO/LAO are subjected, reversely, to compressive in-plane and tensile out-of-plane strains; (iii) third, LCMO forms a coherent interface between substrate and film, while LSMO has a semicoherent one owing to accumulation of the misfit dislocations during deposition.

We have shown that films with a biaxial tensile in-plane lattice strain undergo the magnetic transition at a higher temperature than those with a biaxial compressive strain. This argues that the variation of the Mn–O–Mn bond angle, controlled by the lattice strain, plays a more important role in the formation of the spin ordering in the CMR film than the attendant modification of the Mn–O bond length.

The LCMO/BTO, LSMO/BTO, and LSMO/STO films manifest an in-plane magnetic anisotropy, while the easy-axis magnetization is out-of-plane for the LCMO/LAO and the LSMO/LAO films.

It was shown that the magnetic inhomogeneity, connected with the observed difference in FC and ZFC $M(T)$ dependences, has a metallurgical rather than an electronic nature, and is controlled by the crystal lattice distortion and the microstructure defects.

The observed enhancement of the magnetoresistance effect in the LSMO/BTO bilayered film at room temperature make its greatly beneficial in the development of new hybrid ferromagnetic/ferroelectric devices.

This work was supported by the KOSEF through the Quantum Photonic Science Research Center.

1. J. Volger, *Physica (Utrecht)* **20**, 49 (1954).
2. R. von Helmolt, J. Wecker, B. Holzapfel, L. Schultz, and K. Samwer, *Phys. Rev. Lett.* **71**, 2331 (1993).
3. S. Jin, T.H. Tiefel, M. McCormack, R.A. Fastnacht, R. Ramesh, and L.H. Chen, *Science* **264**, 413 (1994).
4. R.A. Rao, D. Lavric, T.K. Nath, C.B. Eom, L. Wu, and F. Tsui, *Appl. Phys. Lett.* **73**, 3294 (1998).
5. T.K. Nath, R.A. Rao, D. Lavric, C.B. Eom, L. Wu, and F. Tsui, *Appl. Phys. Lett.* **74**, 1615 (1999).
6. J.R. Sun, C.F. Yeung, K. Zhou, L.Z. Zhou, C.H. Leung, H.K. Wong, and B.G. Shen, *Appl. Phys. Lett.* **76**, 1164 (2000).
7. H.S. Wang, E. Wertz, Y.F. Hu, and Q. Li, *J. Appl. Phys.* **87**, 7409 (2000).
8. R. Desfeux, S. Bailleul, A. Da Costa, W. Prellier, and M. Haghiri-Gosnet, *Appl. Phys. Lett.* **78**, 3681 (2001).
9. A. Biswas, M. Rajeswari, R.C. Srivastava, T. Venkatesan, R.L. Green, Q. Lu, A.L. de Lozanne, and A.J. Millis, *Phys. Rev.* **B63** , 184424 (2001).
10. S. Jacob, T. Roch, F.S. Razavi, G.M. Gross, and H.-U. Habermeier, *J. Appl. Phys.* **91**, 2232 (2002).
11. M. Paranjape, A.K. Raychauhuri, N.M. Mathur, and M.G. Blamire, *Phys. Rev.* **B67**, 2144415 (2003).
12. Y.P. Lee, S.Y. Park, V.G. Prokhorov, V.A. Komashko, and V.L. Svetchnikov. *Appl. Phys. Lett.* **84**, 777 (2004).
13. V.G. Prokhorov, G.G. Kaminsky, V.A. Komashko, Y.P. Lee, and S.Y. Park, *Fiz. Nizk. Temp.* **29**, 885 (2003) [*Low Temp. Phys.* **29**, 663 (2003)]; V.G. Prokhorov, V.A. Komashko, G.G. Kaminsky, V.L. Svetch-

nikov, H.W. Zandbergen, Y.P. Lee, J.S. Park, and K.W. Kim, *Fiz. Nizk. Temp.* **29**, 161 (2003) [*Low Temp. Phys*. **29**, 117 (2003)].
14. A.J. Millis, T. Darling, and A. Migliori, *J. Appl. Phys*. **83**, 1588 (1998).
15. M. Bibes, L. Balcells, S. Valencia, J. Fontcuberta, M. Wojcik, E. Jedryka, and S. Nadolski, *Phys. Rev. Lett*. **87**, 67210 (2001).
16. M. Bibes, S. Valencia, L. Balcells, B. Martínez, J. Fontcuberta, M. Wojcik, S. Nadolski, and E. Jedryka, *Phys. Rev.* **B66**, 134416 (2002).
17. V.G. Prokhorov, V.A. Komashko, V.L. Svetchnikov, Y.P. Lee, and J.S. Park, *Phys. Rev.* **B69**, 014403 (2004).
18. V.G. Prokhorov, V.A. Komashko, G.G. Kaminsky, V.L. Svetchnikov, Y.P. Lee, and S.Y. Park, *Fiz. Nizk. Temp.* **30**, 938 (2004) [*Low Temp. Phys*. **30**, 705 (2004)].
19. K.M. Satyalakshmi, S.S. Manoharan, M.S. Hegde, V. Prasad, and S.V. Subramanyam, *J. Appl. Phys*. **78**, 6861 (1995).
20. W. Zhang, W. Boyd, M. Elliot, and W. Herrenden-Harkerand, *Appl. Phys. Lett*. **69**, 3929 (1996).
21. J.-M. Liu and C.K. Ong, *Appl. Phys. Lett*. **73**, 1047 (1998).
22. R. Mahendiran, S.K. Tiwary, A.K. Raychaudhuri, and T.V. Ramakrishnan, *Phys. Rev.* **B53**, 3348 (1996).
23. J. Li, C.K. Ong, J.-M. Liu, Q. Huang, and S.J. Wang, *Appl. Phys. Lett*. **76**, 1051 (2000).
24. V.G. Prokhorov, G.G. Kaminsky, V.A. Komashko, Y.P. Lee, J.S. Park, and H.C. Ri, *Appl. Phys. Lett*. **80**, 2707 (2002).
25. V.G. Prokhorov, G.G. Kaminsky, V.M. Ishchuk, I.N. Chukanova, Y.P. Lee, and K.W. Kim, *Fiz. Nizk. Temp.* **28**, 502 (2002) [*Low Temp. Phys*. **28**, 354 (2002)].
26. G. Srinivasan, E.T. Rasmussen, B.J. Levin, and R. Hayes, *Phys. Rev*. **B65**, 134402 (2002).
27. V.G. Prokhorov, G.G. Kaminsky, V.A. Komashko, J.S. Park, and Y.P. Lee, *J. Appl. Phys*. **90**, 1055 (2001).
28. F. Jona and G. Shirane, *Ferroelectric Crystals*, Pergamon, New York (1962), p. 108.
29. R. Maier and J.L. Cohn, *J. Appl. Phys*. **92**, 5429 (2002).
30. E. Snoeck, B. Warot, H. Ardhuin, A. Rocher, M.J. Casanove, R. Kilaas, and M.J. Hÿtch, *Thin Solid Films* **319**, 157 (1998).
31. Q. Huang, A. Santoro, J.W. Lynn, R.W. Erwin, J.A. Borchers, J.L. Peng, K. Ghosh, and R.L. Greene, *Phys. Rev.* **B58**, 2684 (1998).
32. M.C. Martin, G. Shirane, Y. Endoh, K. Hirota, Y. Moritomo, and Y. Tokura, *Phys. Rev.* **53**, 14285 (1996).
33. O.I. Lebedev, G. Van Tendeloo, S. Amelinckx, B. Leibold, and H.-U. Harbermeier, *Phillos. Mag*. **A79**, 1561 (1999).
34. O.I. Lebedev, G. Van Tendeloo, S. Amelinckx, H.L. Ju, and K.M. Krishnan, *Philos. Mag*. **A80**, 673 (2000).
35. G. Van Tendeloo, O.I. Lebedev, and S. Amelinckx, *J. Magn. Magn. Mater*. **211**, 73 (2000).
36. T. Walter, K. Dörr, K.-H. Müller, D. Eckert, K. Nenkov, M. Hecker, M. Lehmann, and L. Schultz, *J. Magn. Magn. Mater*. **222**, 175 (2000).
37. F. Tsui, M.C. Smoak, T.K. Nath, and C.B. Eom, *Appl. Phys. Lett*. **76**, 2421 (2000).
38. For a review, see E. Dagotto, T. Hotta, and A. Moreo, *Phys. Rep*. **344**, 1 (2001).
39. A.J. Millis, R. Mueller, and B.I. Shraiman, *Phys. Rev.* **B54**, 5405 (1996).
40. A.J. Millis, *Phys. Rev.* **B53**, 8434 (1995).
41. Y.H. Li, K.A. Thomas, P.S.I P.N. de Silva, L.F. Cohen, A. Goyal, M. Rajeswari, N.D. Mathur, M.G. Blamire, J.E. Evetts, T. Venkatesan, and J.L. MacManus-Driscoll, *J. Mater. Res*. **13**, 2161 (1998).
42. J.Z. Sun, D.W. Abraham, R.A. Rao, and C.B. Eom, *Appl. Phys. Lett*. **74**, 3017 (1999).
43. J. Blasko, J. Gareia, J.M. DeTeresa, M.R. Ibarra, P.A. Algarabel, and C. Marquina, *J. Phys.*: *Condens. Matter* **8**, 7427 (1996).
44. J. Hayakawa, H. Asano, M. Matsui, and H. Takahashi, *J. Magn. Magn. Mater*. **84**, 84 (2000).
45. M. Zeise, H.C. Semmelhack, and P. Busch, *J. Magn. Magn. Mater*. **246**, 327 (2002).
46. H.Y. Hwang, S.W. Cheong, N.P. Ong, and B. Batlogg, *Phys. Rev. Lett*. **77**, 2041 (1996).
47. C.M. Varma, *Phys. Rev.* **B54**, 7328 (1996).
48. M. Medarde, M. Mesot, P. Lacorre, S. Rosenkranz, P. Fisher, and K. Grobcht, *Phys. Rev.* **B52**, 9248 (1995).
49. Y. Tokura, Y. Tomioka, H. Kuwahara, A. Asamitsu, Y. Moritomo, and M. Kasai, *J. Appl. Phys*. **79**, 5288 (1996).
50. H.-U. Harbermeier, *Physica* **B321**, 9 (2002).